APPLIED SCIENCE

The research activities categorized as applied science include energy, technology, and the environmental sciences. The projects are perhaps more closely geared towards solving immediate problems than other kinds of fundamental research.

Environmental Science

The application of synchrotron techniques to the area of environmental science has been one of the key areas of development at the NSLS in the last year. Particular progress has been made in the study of waste metals in soils. EXAFS and XANES are among the core techniques applicable towards understanding the typically heterogeneous samples relevant to hazardous waste remediation. For example, M. Szulczewski, W.F. Bleam, and P.A. Helmke (U. of Wisconsin) examined the structure of metal ions in a number of soil environments using the facilities of beamlines X11A and X23B. In one series of experiments, XANES spectroscopy was used to identify the oxidation state of chromium (Cr(III) versus Cr(VI)) in contaminated soil samples (Figure 1). Due to the significant differences in the pre-edge features of various oxidation states of chromium, the presence of the notoriously toxic Cr(VI) can be identified (and accurately quantified) even when the more benign Cr(III) predominates. Other studies by this group have examined a range of first row transition elements in soil, concluding that the elements are bound to humic substances.

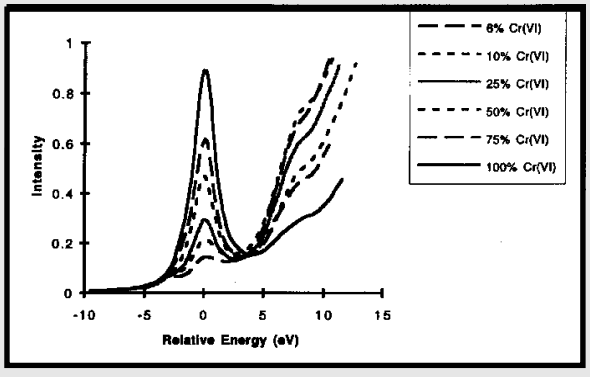

Figure 1: Cr K-edge spectra of the pre-edge region of standard physical mixtures with varying fractions of Cr(VI):Cr(III). (X23B)

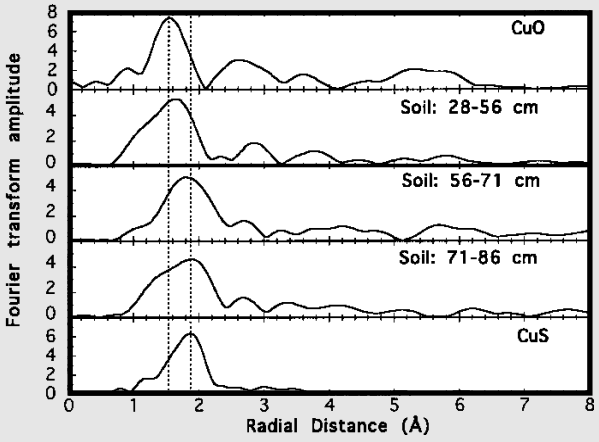

Figure 2: Radial structure functions for Cu(II) in soil samples from different depths and selected standards. Data are not corrected for phase shift. (X11A)

D.E. Sayers, D. Hesterberg, W. Zhou, W.P. Robarge, and G.M. Plummer (North Carolina State U.) have also carried out a number of environmental chemistry of soils studies on beamline X11A. In one investigation, the chemical forms of metals occurring at different depths in contaminated soil in a superfund site were examined, with the hypothesis that redox potential and oxygen availability would play a significant role in metal speciation. The hypothesis was to some degree confirmed, in that analysis of copper EXAFS data showed reduction in Cu-oxygen bonding and increases in copper-sulfur bonding with soil depth (Figure 2). Cu-S was determined to be the primary mineral species in the sub-surface samples.

Another example is the collaboration between K. Xia, F. Weesner, W.F. Bleam (U. of Wisconsin), P.R. Bloom, and U.L. Skyllberg (U. of Minnesota), who carried out sulfur K-edge XANES studies on beamline X19A to characterize the oxidation states of sulfur in both soil and aquatic environments. They identified six major sulfur containing functional groups in humic material and demonstrated the ability to distinguish sulfur oxidation states in aquatic, organic, and mineral soils.

Trace metals in the environment are important for their effects on biological systems, and so these element-specific techniques are particularly interesting when applied to organisms. The x-ray fluorescence microprobe was used to study a number of problems of environmental importance, including measurements of trace Pb in bone by C.S. Fullmer (Cornell U.) and K.W. Jones (Brookhaven National Laboratory). These studies, on chick tibia, investigated how lead affected bone growth by studying Ca and Pb distributions in normal and calcium deficient bones. Another study of metals in tissue was that undertaken by W.J. Berry, D.J. Borsay (U.S. Environmental Protection Agency) and K.W. Jones (BNL) of marine organisms living in sediments. In this case, the location of absorbed metals could be established for clam worms exposed to metals in controlled ways. Additionally, samples of dredged material from the NY/NJ harbor were studied by K.W. Jones (BNL) and S.-R. Song (BNL and Yale U.). By screening for contaminants as a function of sample particle size it was possible to check whether a simple physical separation method could be useful in decontaminating such materials. It was found that contaminants were present for all particle sizes at about the same concentration. A somewhat related experiment was performed by T.K. Tokunuga, S. Bajt (Lawrence Livermore National Laboratory) and G. Shea-McCarthy (U. of Chicago) on the oxidation state of selenium in sediments, decomposing plant residue and algae. These studies are of interest because the toxicity of selenium is highly related to its oxidation state.

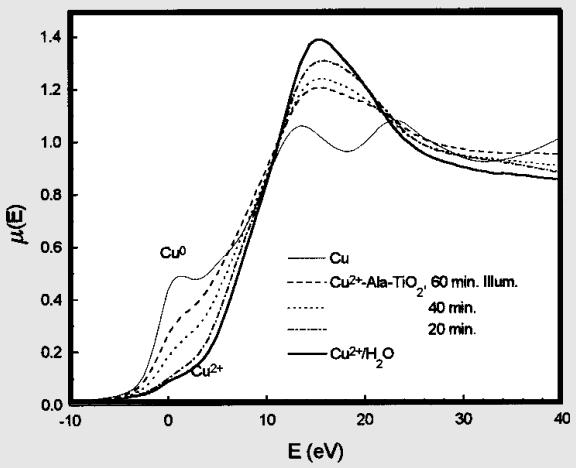

Figure 3: XANES of Cu^{+2} as a function of illumination time in the TiO_2 catalyzed photoreduction with alanine derivatization. (X18B)

Energy Conversion and Storage

Environmental systems are interesting not only from the life science point of view, but also as mechanisms for efficient energy and chemical conversions. There is perhaps no better example than photosynthesis, the natural harvesting and ultimate storage of solar energy. Researchers have been studying a variety of simpler systems, such as nanoclusters, for potential applications in photochemistry and electronics. For example, L.X. Chen, T. Rajh, D.M. Tiede, P.A. Montano, and M.C. Thurnauer (Argonne National Laboratory) studied titanium oxide clusters on beamline X18B. When photoirradiated, these semiconductor particles produce charge separation on their surfaces. They can thus act as electron donors or acceptors in oxidation/reduction reactions with molecules in their surrounding media, making them interesting for environmental remediation applications. The researchers studied the titanium k edge EXAFS on clusters of varying sizes and found systematic variations as the ratio of surface to bulk atoms changes. They studied the photoreduction of Cu^{+2} ions on the TiO_2 colloid surface with and without surface derivatization with alanine. They were able to confirm the production of Cu^0 and could see complexes between copper ion and alanine as seen in Figure 3 along with their time dependence. Further studies were also carried out with mercury ions, which are environmentally relevant.

One of the important technological challenges is the development of inexpensive and efficient means of energy storage. The advent of more and more portable electronics, not to mention electric vehicles, is continuing to press the development of new battery technologies. The central obstacles in these developments are, of course, materials questions. T. Thurston, N.M. Jisrawi, S. Mukerjee, X.Q. Yang, J. McBreen (Brookhaven National Laboratory), M.L. Daroux, and X.K. King (Gould Electronics) have continued to exploit the high energy diffraction capabilities of beamline X27A for *in situ* structural characterization of working $Li_xMn_2O_4$ batteries. With measurements made through the external case, electrolyte, and binding materials, the experimenters were still able to collect diffraction patterns at reasonable count rates. The researchers found, among other results, evidence for coexisting phases over a range of voltages.

In work on X23A2 and X23B, P.E. Stallworth (U.S. Naval Academy), M.L. denBoer, S. Kostov, and S. Greenbaum (Hunter CUNY) also investigated the properties of lithium based battery cathodes. In systematic studies of $Li_xV_6O_{15}$ {x=0,0.5,1,1.5,2,3,4,5,6} carried out with NMR techniques to determine the environment of the intercalated lithium and XAS to determine the local

environment of the vanadium, the researchers found several structural regimes as a function of x. Using both the near edge quadrupolar peak intensity and the EXAFS as measures of the degree of symmetry of VO_6 octahedra, the team found a region of slight increase in the distortion from O_h with $0<x<1$, followed by a region of rapid increase in asymmetry for $1<x<3$, finally followed by a region of only small change. This is illustrated in Figure 4(a) which shows both the XANES and EXAFS results. The NMR evidence suggests that Li enters a single site at the lowest concentrations, but a variety of sites at the higher ones. The disorder extends beyond the first shell [Figure 4(b)], as evidenced by a decline in the outer shell amplitudes relative to the first shell.

(a)

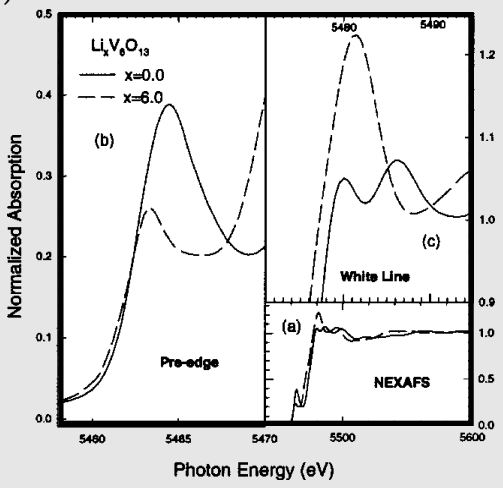

Figure 4: (a) Representative vanadium K-edge x-ray absorption spectra for a few compositions of $Li_xV_6O_{13}$ battery cathode materials. (X23A2, X23B)

(b)

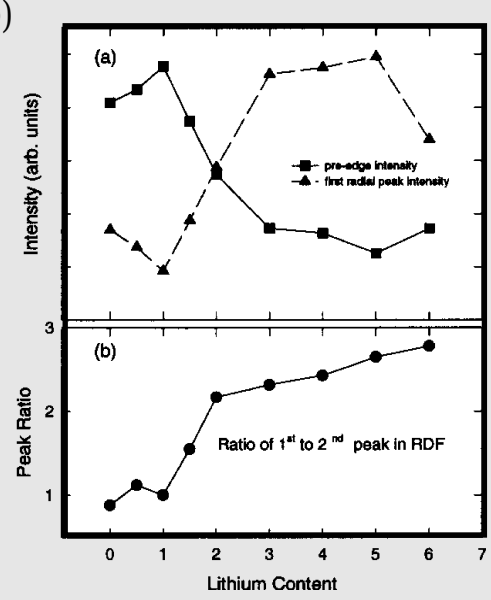

(b) The vanadium 1s-3d pre-edge transition intensity for $Li_xV_6O_{13}$ as a function of x.

Superconductivity

Superconducting wires and tapes made with high-T_c cuprates are a prime example. Such wires are typically a composite mixture of $Bi_2Sr_2Ca_2Cu_3O_x$ (Bi-2223) with silver, processed to yield a high critical current at a particular operating temperature. Like many of the cuprates, the superconducting properties of Bi-2223 are robust only for transport along the Cu-O planes, making grain orientation a key factor in determining the critical current density. For example, T.R. Thurston, W. Wildgruber, N.M. Jisrawi, M. Suenaga, Y.L. Wang (Brookhaven National Laboratory), and P. Halder (IGC Corporation) continued to exploit the high energy powder diffraction capabilities of beamline X27A for *in situ* characterization of Ag-clad Bi-2223 high-temperature superconducting wires. In the experiment shown in Figure 5, the phase and texture development of Bi-2223 are monitored as it is generated from precursor materials (Bi 2212 + CuO) within its silver sheath. The reaction was driven in a series of temperature steps at 600° and 840°C. The researchers found that the formation of the Bi 2223 phase and the overall texturing were decoupled processes.

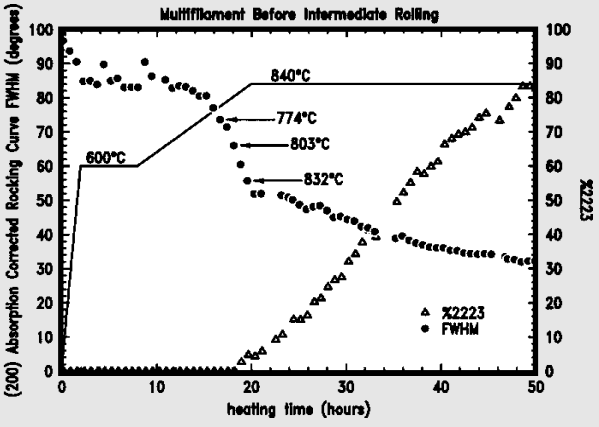

Figure 5 : Time dependence of the phase and texture development in a multifilament wire. (X27A, X22A)

Electronic Materials

The rapid developments in the electronics and semiconductor industries provide ample motivation for materials studies. There are many important problems which require diffraction information from areas of a few square microns or less within a patterned sample, for example a semiconductor device and its interconnections. There have been several such microdiffraction experiments performed at the NSLS this year, with significant technical applications. E.D. Isaacs, K. Evans-Lutterodt, M.A. Marcus, A.A. MacDowell, W. Lenhart, L.J.P. Ketelsen, J. Vandenberg, W.T. Tsang, J.E. Johnson, J.A. Grenko, and S. Sputz (Bell Laboratories) have produced a 5 micron monochromatic spot, and used it for studies of patterned InP multi-quantum well (MQW) lasers. The variation in MQW period and strain as a function of position across the fabricated structure is clearly seen in the data of Figure 6. These measurements could only be made with x-rays since these structures are buried and thus inaccessible to electron diffraction measurements.

In a somewhat different approach, G.S. Cargill, P.-C. Wang (Columbia U.), I.C. Noyan, E.G. Liniger, C.-K. Hu, and K.Y. Lee (IBM Research) used a tapered capillary to obtain a 10 micron white x-ray beam and measured a diffraction pattern with an energy dispersive detector at X26C. They applied their setup, the first real-time strain measurements permitting such fine spatial resolution, to the study of electromigration and annealing in aluminum interconnect lines. Due to the stability and reproducibility of the detector in terms of peak shape and the use of an *in situ* tungsten standard, peak positions were easily measured to within 1% of the peak width. This was sufficient to directly deduce the strain induced from the electromigration in the aluminum interconnects under study.

H.Y. Lee (Synchrotron Radiation Research Center), C.H. Lee (Nat. Tsing Hua U., Taiwan), and K.S. Liang (Exxon) made *in situ* measurements of sputter-deposited thin films of $LaNiO_3$ on X22A. This material is an interesting substrate for integrated ferroelectric capacitors for microelectronic applications. They found that the material first deposits as an amorphous film, of about 100 Å thickness. Another application of x-ray analysis to very thin films was made by C. Kim, I.K. Robinson, J. Myoung, K.-H. Shim, and K. Kim (U. of Illinois) on X16C, where they studied the evolution of the in-plane and out-of-plane lattice parameters of GaN films in the range of 50-10,000 Å.

Metal silicides are potential candidates as contact materials in advanced semiconductor applications, but many fundamental issues of resistivity and stability

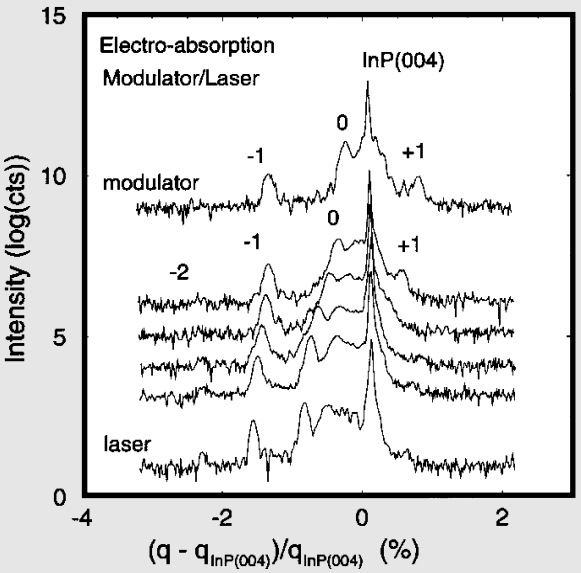

Figure 6: Radial Bragg scans along the InP(004) substrate direction taken at positions inside the laser structure (bottom line), through the transition region (middle four lines) and into the modulator region (upper line) taken with 5 μm spatial resolution. The variation in MQW period and strain as a function of position is observed as a variation in spacing between superlattice peaks (labeled by order) and the position of the other order peak, respectively. The data are offset for clarity. (X16C)

remain to be investigated. Z. Wang, P.T. Goeller, B.I. Boyanov, D.E. Sayers, and R.J. Nemanich (North Carolina State U.) designed, constructed and tested a UHV system for *in situ* studies of structures grown on semiconductor wafers via electron-beam evaporation. In first EXAFS measurements on beamline X11A (at the Co k edge) on cobalt and silicon codeposited and annealed in a 1:2 stoichiometric ratio on $Si_{0.8}Ge_{0.2}$ films, the researchers found evidence for the formation of stable cobalt silicide ($CoSi_2$). At annealing temperatures below 600° C, there was evidence as well for presence of a small amount of CoSi. The UHV chamber permits full characterization with a variety of techniques in addition to XAS. These include AES, XPS, UPS, RHEED, and ARXPS/UPS, and it is again appropriate to point out that well conceived XAS science backs up conclusions with corroboration by as many methods as possible.

InP is an important semiconductor material for long wavelength optoelectronic devices and high frequency electronic devices. The performance of these devices is controlled by the structural and chemical

uniformity of the epitaxial layers, which in turn, is strongly dependent on the structural perfection and compositional homogeneity of the substrates on which they are grown. It is, therefore, imperative to improve the crystalline quality and homogeneity of InP substrates. However, the relatively low yield stress of InP makes it susceptible to deformation by stresses generated during crystal growth, making it difficult to produce InP crystals with low dislocation density. In addition, temperature fluctuations imposed by turbulent convective flow give rise to uncontrolled variations in the local solidification rate and in diffusion layer thickness, leading to microscopic and macroscopic chemical inhomogeneity.

In work aimed at studying and improving the growth of InP and other semiconductor crystals, V. Prasad, H. Zhang, M. Dudley, H. Chung, and W. Si (SUNY @ Stony Brook), D.F. Bliss (Air force Rome Laboratories), and A. Maniatty (RPI) have been correlating defect microstructures and interface shapes observed using Synchrotron White Beam X-ray Topography (SWBXT) with the theoretical predictions of heat transfer and stress generation during the single step, high pressure Kyropoulos growth of doped InP boules. This enables a correlation between observed defect structures and both the growth parameters and modeling predictions. The results can provide feedback to the crystal grower to enable optimization of these growth parameters.

Figure 7(a) is a transmission x-ray topograph recorded from a S doped InP crystal. Numerous slip bands (S) nucleated from the cylindrical outer surface of the boule and propagating into the interior of the crystal were revealed. In the growth of indium phosphide, boric oxide is used as an encapsulant to prevent the decomposition of the melt. The encapsulant also reduces the radiative heat loss from the outer surface of the crystal since B_2O_3 acts as a heat shield. Detailed heat transfer modeling reveals that the maximum heat loss occurs at the point where the hot solid material emerges from the encapsulant giving rise to maximum temperature gradients in this region. X-ray topographs revealed that slip bands are most likely to be nucleated at this stage to relieve the large thermal stresses. The distribution of excess resolved shear stresses in the crystal at various stages in the growth process has been calculated using an anisotropic thermo-elastic finite element model for InP single crystals. The result is shown in Figure 7(b). It is worth noting that the maximum excess resolved shear stresses are generated on the outer surface of the crystal at the point where the crystal emerges from the encapsulant corresponding to the region with maximum temperature gradients. The calculated result is in good accord with the slip band distributions revealed by x-ray topography.

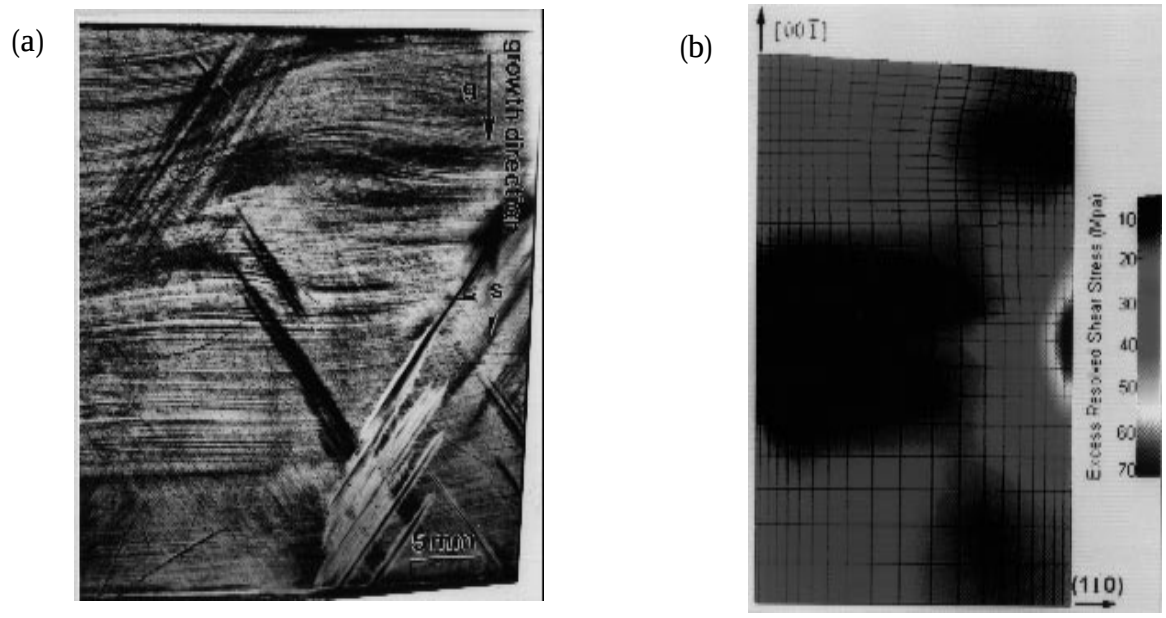

Figure 7: (a) Synchrotron White Beam X-ray Topograph (g=004, λ=0.45Å) recorded in transmission geometry from a longitudinal cut (110) S doped InP wafer showing the distribution of slip bands (S) and (b) the distribution of the total excess resolved shear stress on the (110) plane through the center of the crystal subject to an intermediate growth stage temperature field. (X11A)

Silicon Carbide (SiC), is a very promising semiconductor material for high temperature, high power, and high frequency electronic devices owing to its excellent thermal and electrical properties. One key issue for the fabrication of these devices is the availability of epitaxial layers with high crystalline quality, good dopant homogeneity, and good reproducibility. However, SiC has over 200 polytypes with different properties. Since these polytypes coexist over a wide range of temperatures, obtaining single crystals of large size, containing only one designated polytype is often difficult. In the case of 4H-SiC epitaxial growth on (0001) substrates, one of the big obstacles is the occurrence of triangular inclusions in the epilayer. One method of preventing the formation of triangular inclusions during epitaxial growth is to use substrates misoriented from (0001). The vicinal surfaces of such off-axis substrates provide high densities of surface steps. which facilitates epitaxial growth on such surfaces proceeding through a step-flow mechanism. However, in 4H-SiC epitaxy, the occurrence of triangular inclusions was still found to persist even when substrates misoriented by 3.5° from (0001) were used, although their numbers decreased drastically as the misorientation angle approached 8°.

C. Carter, J. Sumakeris, and H.S. Kong (Cree Research Inc.), and W. Si and M. Dudley (SUNY @ Stony Brook) carried out a detailed study of 4H-SiC epilayers grown on 4H-SiC substrates. Synchrotron White Beam X-ray Topography (SWBXT) and Nomarski Optical Microscopy (NOM) have been used to study the character of triangular inclusions in 4H-SiC epilayers (0001) 4H-SiC substrates with misorientations ranging from 3.5° to 8°. X-ray diffraction pattern analysis carried out on an epilayer grown on a 3.5° misoriented substrate reveal that there are two additional phases, 3C(I)-SiC and 3C(II)-SiC, present in the 4H-SiC epilayer associated with the triangular inclusion. The detailed correlation between the NOM micrograph and reflection topographs is shown in Figure 8 (a) to (d). Evidently, all triangular inclusions belong to one or the other of the two 3C-SiC structural configurations. Most of the triangular inclusions are single crystal 3C-SiC, although they appear to be severely strained. There is only one triangular inclusion consisting of both 3C(I) and 3C(II)-SiC, which indicates the existence of a double position boundary (DPB) within the inclusion. This research shows unambiguously that the triangular defects observed in the 4H-SiC epilayers studied are 3C-SiC inclusions.

It is well known that in 4H-SiC single crystal substrates, there exist superscrew dislocations along the <0001> axis whose Burgers vector magnitudes are equal to a multiple of the c lattice constant (c = 10.05 Å). Figure 9 (see next page) shows (a) a NOM micrograph of an epilayer grown on such a substrate and (b) a back-reflection topograph. Triangular inclusions (TI), growth pits (P), and scratch (S) marks are observed on the micrograph. The directions from the apex of the triangle to the base are <-1 2 -1 0> directions, which correspond to the down-step directions (direction of lateral step growth). The length of altitude from base of the triangle to the peak is around 97 to 120 microns. The density of growth hillocks is $3 \sim 4 \times 10^4$ /cm^2, and the diameter is around 1 micron. Superscrew dislocations including micropipes (M) and elementary screw dislocations (ED) show circular white features on the topograph. By comparison, it is evident that there is no obvious correlation between superscrew dislocations and 3C-SiC triangular inclusions. Also there is no evidence showing that the growth hillocks are related to the superscrew

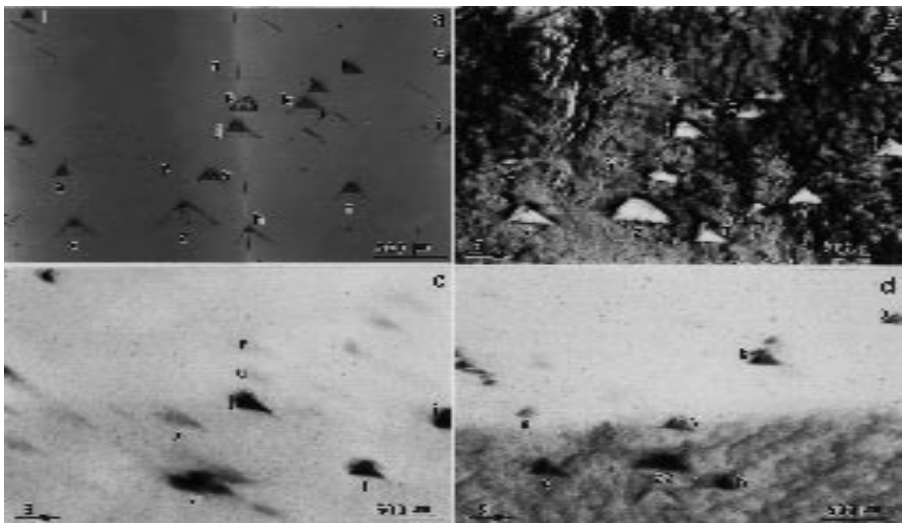

Figure 8: 4H-SiC epilayers on 4H-SiC substrates misoriented by 3.5° from (0001), (a). a NOM micrograph, (b). the reflection topograph from the same region, 4H-SiC, g = 1-1 0 6, λ = 0.78 Å, (c). the reflection topograph of 3C(I)-SiC, g = 202, λ = 0.91 Å, and (d). the reflection topograph of 3C(II)-SiC, g = 131, λ = 0.67 Å. (X11A)

dislocations since the density of growth hillocks is one order of magnitude higher than that of superscrew dislocations (~$10^3/cm^2$).

Magnetic Materials

Magnetic materials, particularly thin film structures, find immediate application in magnetic recording media for computer and entertainment applications. Several experiments of technical importance were carried out in the past year. Fe-Cr superlattices are of interest because of their giant magnetoresistance, but this effect depends strongly on the preparation conditions. W. Dmowski and T. Egami (U. of Pennsylvania) used beamline X7A to study the interfaces of sputtered films, and inferred that roughness at relatively short length scales increases the magnetoresistance.

T.R. Thurston, L.H. Lewis, U. Wildgruber, D.O. Welch (Brookhaven National Laboratory), and V. Panchanathan (Magnequench International) used X27A to characterize the texture distribution in thermomechanically deformed $Nd_2Fe_{14}B$ magnets. This type of work is still relatively new at synchrotron sources, and is representative of a wealth of potential applications which will increasingly appear at the NSLS. L.H. Lewis, C.H. Sellers (Idaho National Engineering Laboratory), and V. Panchanathan(Magnequench International) have also studied $Nd_2Fe_{14}B$ magnets, using X7A to determine the phases present in the multiphase samples which result from rapid solidification.

Q. Zhu (Brookhaven National Laboratory) used beamline X7A, to study the increase in the structural order parameter in the soft magnetic alloy Fe-Co-V with thermal aging, and was able to identify a minority phase comprising only 0.3% of the sample. The results call into question the widely-accepted belief that a fully ordered Fe-Co alloy exhibits the optimal magnetic properties.

Properties of Materials

X-ray scattering techniques are an old and established probe of structural properties of bulk matter. They can detect the presence of small amounts of a second phase in nominally single phase systems, residual strain, the existence of precipitates, etc. Thus these techniques remain fundamental to understanding details of technologically relevant problems in ceramics and alloys, for example.

The X3A2 beamline was used by Y. Gao, W. Hasz, and C.A. Johnson (GE Corporate Research and Development) for a spatially-resolved crystallographic study of yttria-stabilized zirconia, oriented toward the development of x-ray diffraction techniques to derive the temperature history of a ceramic sample. A. Sahiner, D. Wittmer, and M. Sweeney (S. Illinois U.) used the same beamline to study the effects of thermal shock on the residual stress of Si_3Ni_4 ceramic composites. They found that the compressive stress decreases as the temperature is increased above 1130°C, becoming a tension in the in-plane direction at 1400°C.

The tunability of synchrotron radiation has been used to advantage by D. Alexander (APS, Argonne) on X6B to study defects in steels used in reactor pressure vessels. For example, using anomalous small angle scattering it was possible to identify CuMn precipitates in a Fe-Cu-Mn alloy. Such precipitates are known to cause embrittlement in alloys.

Polymers and Polymer Composites

Polymer composites take many forms, depending on the application. Structural composites, such as Nextel fibers in ceramic matrices and carbon fibers in polyamide, are being investigated by R.J. Meilunas and A. Tobin (Northrop Grumman) at beamline U2B. Some of these

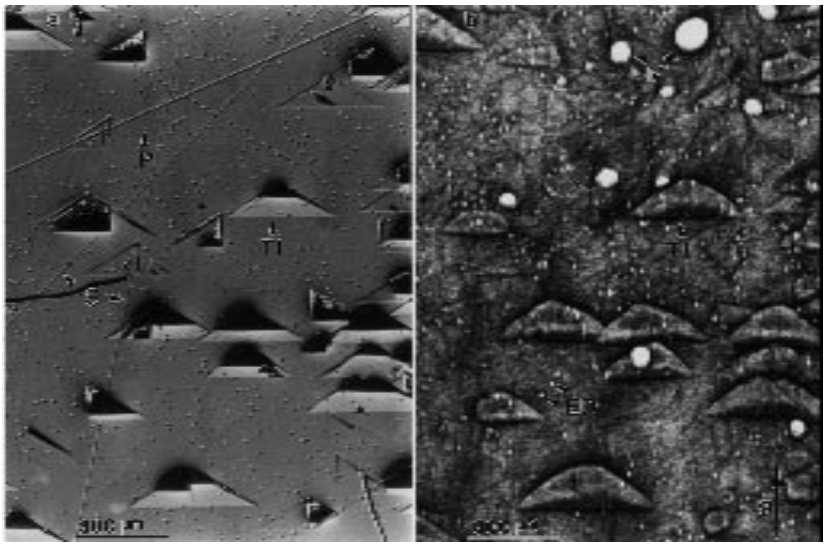

Figure 9: 4H-SiC epilayers on the 4H-SiC substrates misoriented by 3.5° from (0001), (a). a NOM micrograph, and (b) the back-reflection topograph recorded from the same region, g = 00024, λ = 0.83 Å. (X11A)

composites are intended for use in hostile environments (elevated temperatures, oxidative atmospheres, etc.) and the local chemistry (e.g. at the fiber - host matrix interface) controls many of the desired properties. By performing IR microspectroscopy on such localized regions, Meilunas and coworkers have identified fiber sizings (coatings) that inhibit thermo-oxidative degradation of the surrounding matrix.

Another type of polymer composite is in the form of laminates. The layers are frequently a few microns to several tens of microns in thickness, depending on the laminate's intended purpose e.g. photographic film emulsion or food container. In the latter case, the various layers provide the proper combination of structural integrity, sanitary surfaces, and barriers against penetration by light or gases. Much thinner layers are used in photographic emulsions. However, in both cases the interdiffusion of chemicals between the layers must be understood and controlled. Several studies of this nature have been conducted, including one study of a laminated polymer used for plastic containers. Figure 10 shows such a laminate in cross section, and a linear spectroscopic absorption map. While the optical image of the microtomed section suggests a clear delineation of the layered materials, the infrared map provides evidence of chemical diffusion. This is especially apparent between layers 3 and 4 where the absorption features in the "fingerprint region" (below 1500 cm^{-1}) show an overall gradient from the interface to a depth of 10 mm or more into layer 4. Similar behavior is seen, though to a lesser extent, between layers 2 and 3.

In a collaboration between D.L. Wetzel (Kansas State U.) and R.O. Carter (Ford Science Research Center), degradation profiles from photochemical reactions, were measured into the surfaces of acrylic polymers with and without polyethylene or polypropylene protective surface coatings. Cross sections of the exposed acrylic were microtomed and measured in transmission. The unprotected acrylic materials showed damage that extended from the surface to a depth of about 20 microns. In particular, the absorption signatures for the acrylic were weak at the surface. Actual photochemical reaction products (OH, carbonyl) were detected several microns into the surface. Measurements of protected acrylic material showed no evidence of damage, even near the surface.

A considerable number of measurements were made at X1A by H. Ade, A.P. Smith, T. Coffey (North Carolina State U.), and collaborators both on mixtures of copolymers and polymers and on laminate structures, further demonstrating the capability of the technique as an analytical tool. The morphology and composition of a macrophase separated blend of poly[(styrene-r-isoprene)'-b-(styrene-r-isoprene)" random block copolymer (RBC) (20%) with homopolystyrene (PS) (80%) was investigated and micron sized ellipsoidal dispersions of the RBC were found within the matrix. Polycarbonate styrene-acrylonitrile copolymer blends grafted on to polybutadiene and titanium oxide were also studied. In another example, the spinodal decomposition of two polymers PS/PMMA constrained to a surface was imaged and showed segregation of the PS into spheroids within the PMMA matrix. Studies were also made of polymeric isomers, which could be distinguished spectroscopically due to the differences in the local chemical environment. Finally, to ensure that radiation damage was not a problem in these experiments, radiation damage experiments were carried out on PET up to 2.7 Mrad.

Figure 10: Laminated plastic material investigated by scanning IR microspectroscopy. (Top) A description of the plastic layers, their purpose and respective thicknesses. (Bottom) Linear scanned IR absorbance map across a 6 mm thick microtomed section. Also shown is a photographic image of the section, and labels for the various layers. (U2B)

Projection Lithography

A. MacDowell and O. Wood II (Lucent Technologies) continued phase-measuring, lateral shearing interferometry on a multilayer-coated extreme ultraviolet (EUV) imaging system using 13.5 nm radiation from the U13 undulator. This common-path interferometer addresses one of the major challenges confronting EUV lithography, namely the lack of wavefront measuring metrology at the multilayer coating's operational wavelength.

Experimentally a 0.08 NA subaperture of a 10:1 reduction Mo/Si multilayer-coated Schwarzschild camera is illuminated by 13.5 nm radiation emerging from a 4.5 micron pinhole. An open-stencil amplitude grating, with period chosen so that the lateral shear between diffracted orders is small enough that multiple-beam interference can occur in the region of overlap, is positioned in the camera's image plane. A phase-shifting technique, in which a CCD detector is used to record 13 interferograms produced by shifting the grating in the shear direction one twelfth of its period, is used to determine the difference in phase between the two interfering wavefronts. Phase difference data from the same wavefront recorded with shears in orthogonal directions are combined using a method involving least squares to produce a two-dimensional phase map of the camera's wavefront, as shown in Figure 11. The measured wavefront error over the camera's aperture after piston, tip, tilt and defocus have been removed is 0.098 waves RMS at a wavelength of 13.5 nm. While this value only slightly exceeds the Marechal condition (0.071 waves RMS), for "diffraction-limited" imaging, the wavefront errors in an imaging system for production EUV lithography will have to be considerably smaller. Since the sensitivity of this lateral-shearing interferometer was shown in earlier experiments to be better than 0.021 waves RMS at 13.5 nm wavelength, even in its current state of development it can be used to evaluate the image quality and improve the alignment of existing EUV imaging systems.

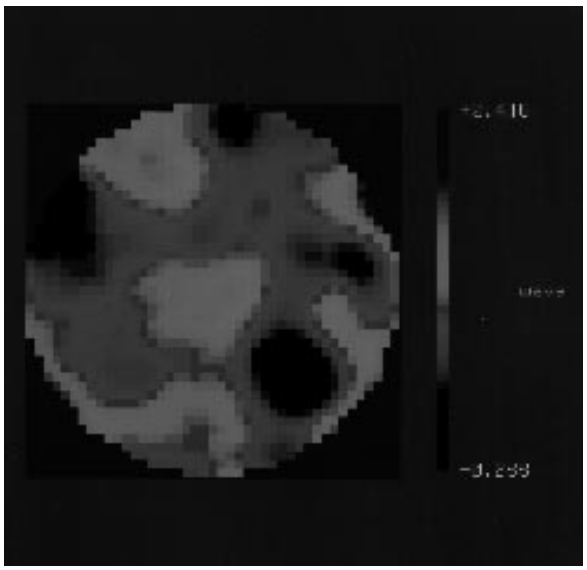

Figure 11: A two-dimensional phase map of the U13 camera's wavefront obtained by combining phase difference data from the same wavefront recorded with shears in orthogonal directions. the measured wavefront error over the camera's aperture after piston, tip, tilt, and defocus have been removed is 0.098 waves RMS at a wavelength of 13.5 nm. (U13)

Hard X-Ray Lithography

To extend lithographic techniques to structures thicker than 0.5 mm it has been shown to be beneficial to employ a hard x-ray source such as the NSLS X-Ray Ring. The NSLS has established a program in this area currently located at X27B which is centered on exposure technique development. They have succeeded in manufacturing precise fully figured 3-dimensional objects on a length scale of many millimeters. So far, the material of choice as a resist has been polymethyl-methacrylate (PMMA) since it is well know in other lithographic applications. In the present protocol, x-ray exposed areas are subsequently removed in a selective solvent system. To produce a pattern on the resist, an x-ray opaque mask is placed in front of a resist sample. The mask and sample are scanned together vertically through the x-ray beam. Often filtering is employed to tailor the high energy cutoff of the beam to the particular application, and parameters such as scan rate, total dose, and substrate temperature are controlled to manipulate the exposure. The patterning masks used to date have included shadow masks assembled from thick high Z materials (tool blocks and rods for example), and in collaboration with H. Guckel *et al.* (U. of Wisconsin), 50 micron thick patterned gold absorber on silicon wafers; objects which are themselves lithographically produced. Figure 12 (see next page) shows an example of the finish provided by hard x-ray lithographic exposure (the side walls) as compared with conventional diamond machining (the front face of the PMMA). It also exhibits faithful reproduction of the mask features (crisp corners and defects) and no observable runout from the front of the resist to the wafer surface.

To facilitate prototype hard x-ray exposures, the NSLS group developed a controlled aperture system which allows objects to be directly written. The aperture consists of two pairs of molybdenum rods mounted on actuators which compensate for beam induced heating. They can be moved under computer control to form rectangular apertures of arbitrary height and width anywhere within the 40 mm fan of beam available from X27B. By placing the sample on a rotary stage coupled to a vertical scan stage, objects of arbitrary shape and orientation can be patterned. Figure 13 shows an SEM image of a series of long channels in 1 mm PMMA sheet produced with one axis of the writer. An array of 50 channels were machined that are 40 mm long, 125± 3 mm wide, placed 500 mm apart. In order to produce longer channels and multiple wafer exposure, a long-throw scanner was built for X27B. It has a stroke of over 600 mm, and can scan at rates over 250 mm/s. This high speed has proven useful for exposure parameter studies, in particular fixing not only the total dose, but the dose rate received in an exposure. The whole system has been automated with a Labview based control system. The scanner has proven sufficiently reliable and robust that it is being duplicated for the new X14B exposure station.

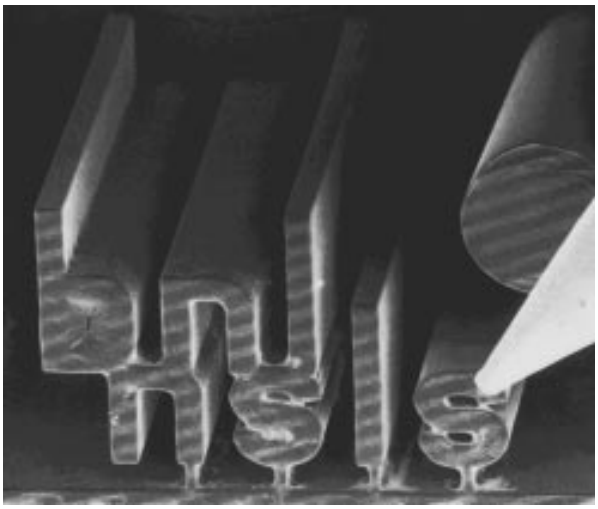

Figure 12: Lettering in 1 mm thick PMMA sheet. At right is the point of a tailor's pin. Note the smooth side walls as compared of the conventionally diamond machined surface of the acrylic sheet. (X27B)

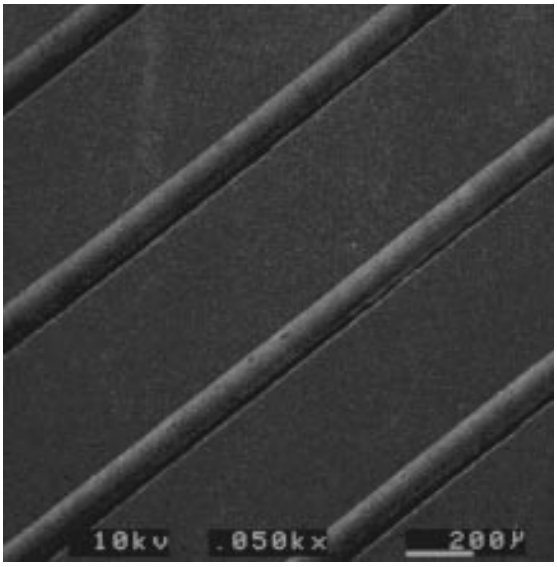

Figure 13: 125 micron wide tracks in 1 mm thick PMMA sheet. Pitch is 500 microns. (X27B)

This beamline is being built to provide more user access to beam time for prototype production runs. The X14B beamline also provides a roughly 100 mm wide exposure field which should improve throughput over X27B which only has a 40 mm fan of radiation. Expansion of this capability will be important, as some users have already started moving to the next step of device fabrication. For example, J. Song *et al.* (Argonne National Laboratory), used the X26C beamline to pattern resist which was ultimately fabricated into mm-Wave Accelerating Cavities. They electroplated 99.9% oxygen free copper into cavities prepared in PMMA resist by hard x-ray lithography. The assembly was then diamond-lapped to provide a uniform thickness cavity. They have successfully made a 30 cell prototype of a rectangular 108-GHz structure using this technique.

Conclusion

Synchrotron x-rays are ideal tools for applied science. Their penetrating abilities permit *in situ* experiments; their wavelengths are well matched to structures at the atomic scale; and the large number of available photons enable high precision measurements.